

## Mechanical response of rockfills in a simulated true triaxial test: A combined FDEM study

Gang Ma<sup>1</sup>, Xiao-Lin Chang<sup>1</sup>, Wei Zhou<sup>\*1</sup> and Tang-Tat Ng<sup>1,2</sup>

<sup>1</sup> State Key Laboratory of Water Resources and Hydropower Engineering Science,  
Wuhan University, Wuhan, 430072, China

<sup>2</sup> Civil Engineering Department, University of New Mexico, Albuquerque, NM 87131, USA

(Received February 23, 2014, Revised May 30, 2014, Accepted June 05, 2014)

**Abstract.** The study of the mechanical behavior of rockfill materials under three-dimensional loading conditions is a current research focus area. This paper presents a microscale numerical study of rockfill deformation and strength characteristics using the Combined Finite-Discrete Element Method (FDEM). Two features unique to this study are the consideration of irregular particle shapes and particle crushability. A polydisperse assembly of irregular polyhedra was prepared to reproduce the mechanical behavior of rockfill materials subjected to axial compression at a constant mean stress for a range of intermediate principal stress ratios in the interval [0, 1]. The simulation results, including the stress-strain characteristics, relationship between principal strains, and principal deviator strains are discussed. The stress-dilatancy behavior is described using a linear dilatancy equation with its material constants varying with the intermediate principal stress ratio. The failure surface in the principal stress space and its traces in the deviatoric and meridian plane are also presented. The modified Lade-Duncan criterion most closely describes the stress points at failure.

**Keywords:** rockfill; microscale modeling; combined FDEM; stress anisotropy; dilatancy; failure envelope

---

### 1. Introduction

The construction of high rockfill dams is becoming increasingly popular because of easily available construction materials and their inherent flexibility, capability to absorb large seismic energy, and adaptability to various foundation conditions and topography. According to statistics, there are approximately 17 rockfill dams over 150 m high planned for the southwest of China, 7 of which with heights over 250 m. Construction of rockfill dams of these heights presents numerous technical problems; the excessive and uncoordinated deformation of the rockfill dam can impact the duration and cost of the entire project, and even compromise dam safety. Thus, the thorough investigation of the mechanical behavior of rockfill materials is emphasized in current research (Xiao *et al.* 2011). Valuable research on the shear behavior of rockfill materials under the conventional triaxial compression (CTC) stress path has been conducted using the triaxial testing apparatus. However, there is limited data on hand to study the shear behavior of rockfill under

---

\*Corresponding author, Professor, E-mail: [zw\\_mxx@163.com](mailto:zw_mxx@163.com)

complex stress conditions due to the current lack of large-scale true triaxial testing facilities. Numerous test results for the three-dimensional shear behavior of sand are available in the literature (Lade 2006), but these data cannot be easily extrapolated to rockfill materials because rockfill assemblies exhibit different structural characteristics and grain-level properties compared with sand.

Some insights can be gained with an alternative approach: the microscale numerical simulation using the Discrete Element Method (DEM). The reliability of test results can be maximized by using the identical numerical sample in different simulations, with no bias in the initial sample fabric and configuration. Moreover, the simulated true triaxial test can be accurately controlled by following the prescribed loading path and boundary conditions. To date, only a few studies have used DEM to investigate the shear behavior of granular materials under a complex stress path, particularly the effect of intermediate principal stress on the shear behavior (Thornton 2000, Ng 2004, 2005, Mahmud Sazzad *et al.* 2012, Barreto and O'Sullivan 2012). In these studies, DEM simulations of polydisperse spherical particle systems were conducted under constant mean stress with varying  $b$  values;  $b$  describes the relative magnitude of the intermediate principal stress with respect to the major and minor principal stresses. The macro- and micro-response of granular materials was analyzed to investigate the effect of intermediate principal stress on the shear behavior of rockfill materials.

This paper contributes to the qualitative understanding of the mechanical behavior of rockfill materials under three-dimensional stress conditions. Two features unique to this study are the consideration of irregular particle shapes and particle crushability. This study involves an extensive set of numerical simulations of true triaxial tests using the Combined Finite-Discrete Element Method (FDEM). A polydisperse assembly of irregular polyhedra was used to reproduce the representative mechanical behavior of rockfill materials subjected to axial compression at a constant mean stress for different  $b$  values (for a range of intermediate principal stress ratios ranging from 0 to 1).

This paper is arranged as follows. First, the combined simulation approach is outlined. Then, the simulation results are presented in terms of both the deformation and strength characteristics, including the evolution of the stress-strain-dilatancy response, the principal strain relationships, the principal deviator strains, the stress and strain incremental vectors, the stress-dilatancy behavior, and the failure surfaces on the deviatoric and the meridian plane.

## 2. Combined simulation approach

The first hybridization of the discrete method with the continuous method was realized in the Universal Distinct Element Code (UDEC) proposed by Cundall and Hart (1992), and was further developed by Munjiza *et al.* (1995). In the combined FDEM modeling of granular materials, each discrete particle is discretized into a finite element mesh as dictated by FEM. The contact between interacting particles is defined in a manner similar to DEM. The major difference between a pure DEM and a combined FDEM is that the former is based only on the interaction laws, whereas the contact (detection and interaction) between individual bodies and the deformability and fracture of the bodies are considered in the latter (Munjiza 2004). Two significant benefits of using the combined FDEM are that (1) various particle shapes can be easily introduced because both the contact detection and interaction algorithms are based on FE discretization instead of particle geometry and (2) a vast range of alternative (e.g., nonlinear constitutive or internally fracturing)

properties can be introduced for individual particles.

The combined FDEM modeling of rockfill materials is performed utilizing the explicit module of the general-purposed finite element software (ABAQUS/Explicit). The explicit integration scheme and general contact capability of this module make it appropriate for a large number of actual and potential contacts undergoing large deformations. This combined FDEM modeling utilizes the simplest linear contact model with a tension limit for the normal component and a coulomb friction limit for the tangential component. Furthermore, the Mohr-Coulomb model with tension cut-off is employed to consider the particle geometry change due to the frictional attrition (Procopio and Zavaliangos 2005).

### 3. Modeling true triaxial test

#### 3.1 The numerical sample

The assembly representing the rockfill materials consists of 8,927 polyhedral particles. Each particle is randomly generated within an ellipsoid by a specially designed and efficient algorithm (see Fig. 1). The particle diameter ranges from 10 mm ( $d_{\min}$ ) to 24 mm ( $d_{\max}$ ), with a uniform distribution by volume fractions ( $P(d) \propto d^3$ ), giving a mean particle diameter ( $d_{50}$ ) of 14 mm. The particle size distribution for this assembly is shown in Fig. 2. The numerical sample is created by initially generating an array of non-contacting particles randomly located in a 400 mm  $\times$  400 mm  $\times$  400 mm cubic cell. The sample is then compressed isotropically to obtain the target void ratio. By setting the inter-particle friction coefficient to 0.0 during compression, a relatively dense sample with a void ratio of 0.48 is created. The final configuration of the sample is shown in Fig. 3. It is also necessary to check for the possible existence of contact orientation anisotropy due to the mode of the sample preparation. Fig. 4 displays the contact orientation histograms after the preparation process. The degree of anisotropy can be quantified using parameter  $\alpha$  in the following expression (Rothenburg and Bathurst 1989)

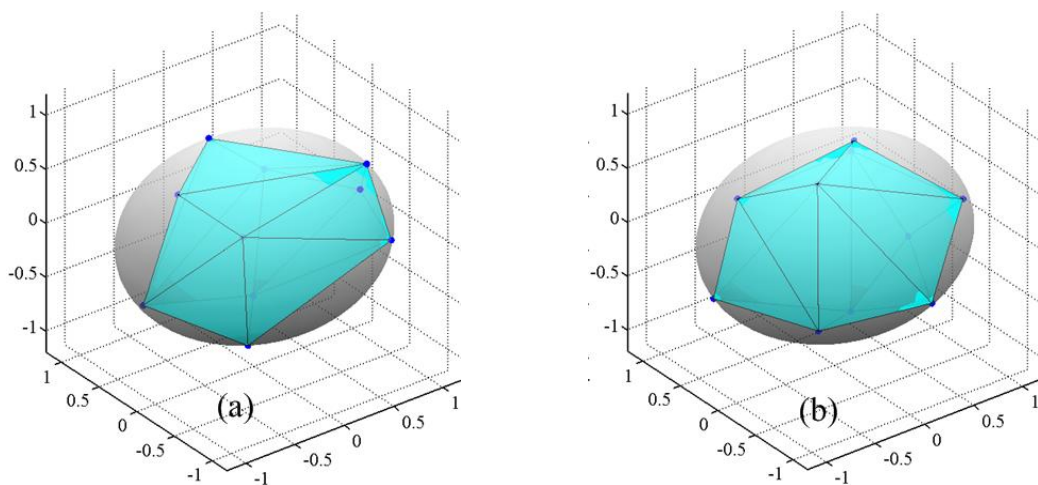


Fig. 1 Two realizations of the particle generation algorithm inside an ellipsoid

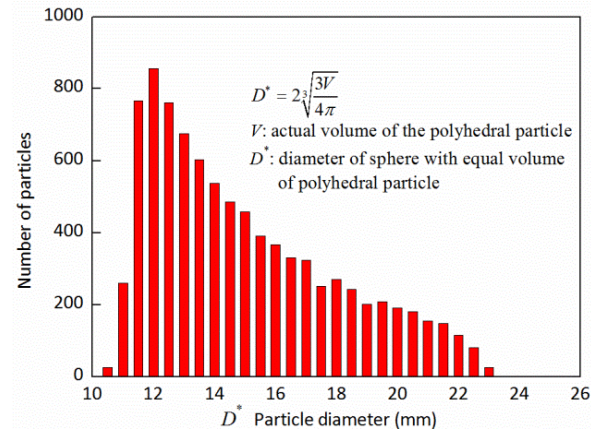


Fig. 2 Particle size distribution

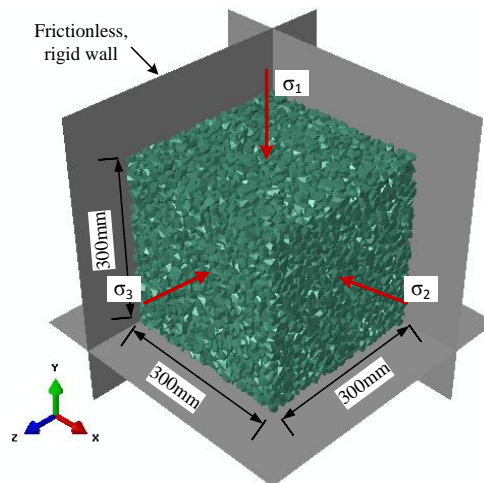


Fig. 3 The numerical sample inside the true triaxial test setup

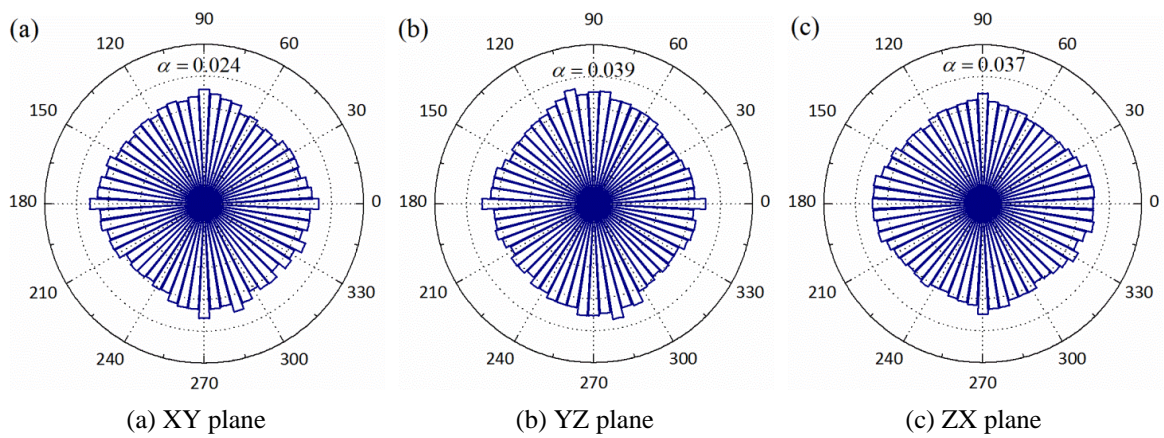


Fig. 4 Distribution of the contact orientation after the preparation process

$$E(\theta) = \frac{1}{2\pi} [1 + \alpha \cos 2(\theta - \theta_0)] \quad (1)$$

where  $\alpha$  is the parameter of anisotropy (a value of zero implies a totally isotropic fabric), and  $\theta_0$  is the major principal direction of the contact orientation anisotropy. The contacts are isotropically distributed and the anisotropy parameters in the XY, YZ, and ZX planes are 0.024, 0.039, and 0.037, respectively, which indicate an almost isotropic state of the sample.

### 3.2 Modeling procedure

Following the sample generation, the numerical sample is initially loaded hydrostatically to a prescribed mean stress  $p$ . Subsequently, the sample is subjected to true triaxial shearing along a specified stress path, while maintaining a constant mean stress. The intermediate principal stress ratio  $b$  is kept constant in each test, where  $b = (\sigma_2 - \sigma_3) / (\sigma_2 - \sigma_3)$  and indicates the relative magnitude of  $\sigma_2$ . The value of  $b$  varies between 0 in triaxial compression and 1 in triaxial extension. The stress paths for these tests are shown in Fig. 5.

Significant variables commonly used to analyze the true triaxial test results are defined as follows: the mean and equivalent deviatoric stress invariants ( $p, q$ ), volumetric and equivalent deviatoric ( $\varepsilon_v, \varepsilon_d$ ) strains and the octahedral modulus ( $G$ ), each defined as follows

$$p = (\sigma_1 + \sigma_2 + \sigma_3) / 3 \quad (2)$$

$$q = \sqrt{\frac{(\sigma_1 - \sigma_2)^2 + (\sigma_2 - \sigma_3)^2 + (\sigma_3 - \sigma_1)^2}{2}} \quad (3)$$

$$\varepsilon_v = \varepsilon_1 + \varepsilon_2 + \varepsilon_3 \quad (4)$$

$$\varepsilon_d = \sqrt{\frac{2}{3} [(\varepsilon_1 - \varepsilon_2)^2 + (\varepsilon_2 - \varepsilon_3)^2 + (\varepsilon_3 - \varepsilon_1)^2]} \quad (5)$$

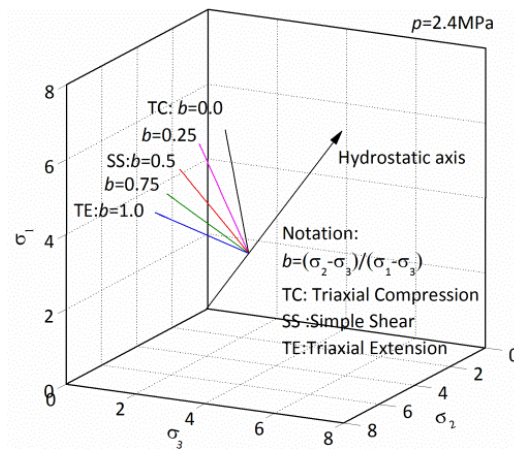


Fig. 5 Stress paths of five true triaxial tests with constant mean stress of 2.4 MPa

$$G = \partial q / \partial \varepsilon_d \quad (6)$$

where  $\sigma_i$  ( $i = 1, 2, 3$ ) are the principal stresses and  $\varepsilon_i$  ( $i = 1, 2, 3$ ) are the principal strains.

### 3.3 Parameter calibration

In a combined FDEM modeling of rockfills, the parameters for FE calculations can be determined by the laboratory tests conducted on the parent rock of blasted rockfill grains. The discrete element parameters, including the inter-particle friction coefficient  $\mu$ , normal and tangential contact stiffness,  $K_n$  and  $K_s$  respectively, need to be calibrated. Thus, a trial-and-error procedure was adopted for the calibration of the micro-parameters such that the numerical simulation yields macroscopic behavior similar to that of laboratory tests reported by Yangtze River Scientific Research Institute (Cheng *et al.* 2010). After a series of trials, the final simulation

Table 1 Set of parameters used in the simulations

|   | Parameter                                   | Value |
|---|---|-------|
| Basic parameter   | Mass density ( $\text{kg/m}^3$ )            | 2600  |
|   | Elastic modulus (GPa)                       | 30    |
| Finite element related<br>(including the parameters of<br>the Mohr-Coulomb model<br>with tension cut-off) | Poisson's ratio                             | 0.2   |
|   | Tensile strength (MPa)                      | 15    |
|   | Cohesion strength (MPa)                     | 34.97 |
|   | Internal friction angle ( $^\circ$ )        | 45    |
| Discrete element related  | Inter-particle friction coefficient         | 0.40  |
|   | Normal contact stiffness ( $\text{N/m}^3$ ) | 30e9  |
|   | Stiffness ratio $K_s / K_n$                 | 0.5   |
|   | Particle/wall friction coefficient          | 0.0   |

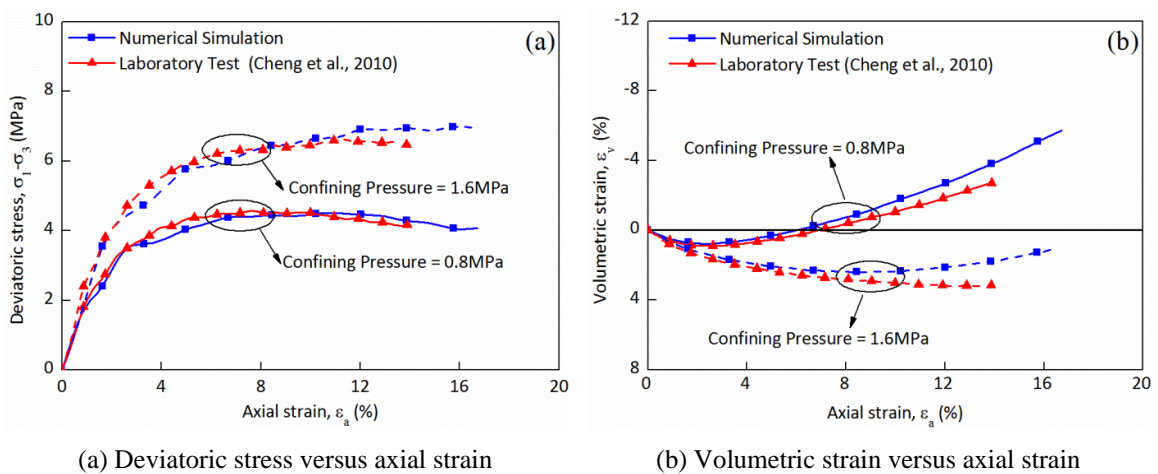


Fig. 6 Parameter calibration by matching the numerical simulation results with experimental reports

parameters are listed in Table 1. Fig. 6 shows the numerical results obtained using the micro-parameters reported in Table 1 for the confining pressures of 0.8 and 1.6 MPa. The results indicate that the non-linear stress-strain behavior of rockfills, including dilatancy, is covered by the numerical model. The combined finite-discrete approach makes it possible to approximately simulate the mechanical response obtained experimentally. These results demonstrate that the model is predictive and can reproduce the typical mechanical behavior of rockfills.

#### 4. Numerical simulation results

##### 4.1 Stress-strain characteristics

A series of combined FDEM simulations of true triaxial tests with constant mean stress ( $p = 0.8, 1.6, 2.4, 3.2, 4.8,$  and  $8.0$  MPa) is conducted by varying  $b$  from 0 to 1, with a step size 0.25. For each test, the initial sample configuration is identical and has an initial isotropic fabric. The simulated stress-strain curves, volume changes, and principal strain relationships at a constant mean stress of 2.4 MPa are shown in Figs. 7 and 8. The arrow on each curve indicates the variation trend of  $b$ . It should be noted that the contraction and dilation are presented in the negative and positive, respectively.

As  $b$  increases from 0, the stress-strain behavior becomes increasingly stiff, both the deviator stress and the axial strain to failure decrease (see Fig. 7(a)). The maximum deviator stress is mobilized in the triaxial compression condition where  $b = 0$ , whereas the minimum mobilized deviator stress is observed for  $b = 1$  in the triaxial extension condition. This result is in agreement with all DEM and experimental studies available. Fig. 7(b) illustrates the evolution of the volumetric strain against the major principal strain for different  $b$  values. It clearly reveals that the volumetric response differs depending on the value of principal ratio  $b$ . Following an initial small contraction, the sample consistently behaves in dilation and gradually trends to a stationary value for all stress paths. To further explore the stress-strain characteristics, the deviator stress and volumetric strain are plotted against the deviator strain in Fig. 8. There is a small difference in the

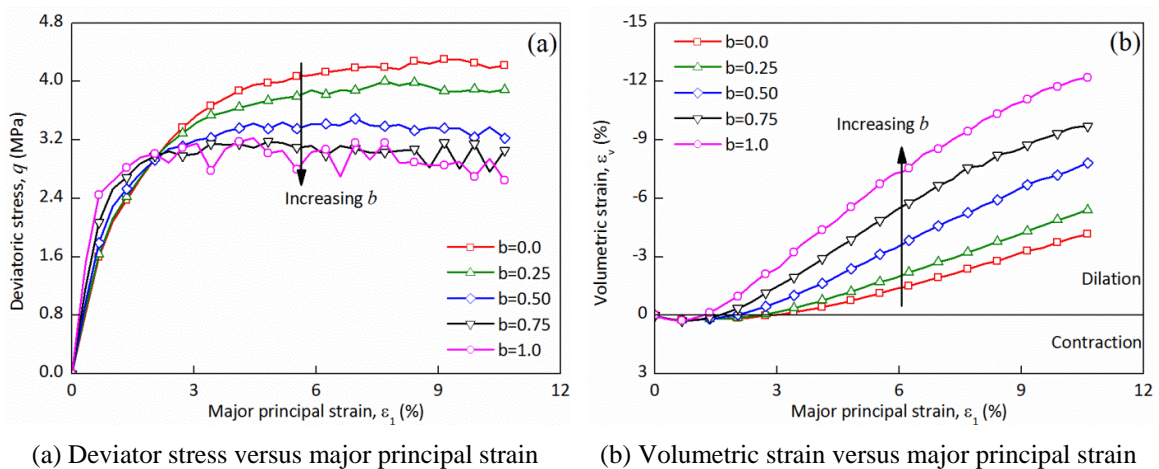


Fig. 7 Simulated behaviors for different  $b$  values with constant mean stress of 2.4 MPa

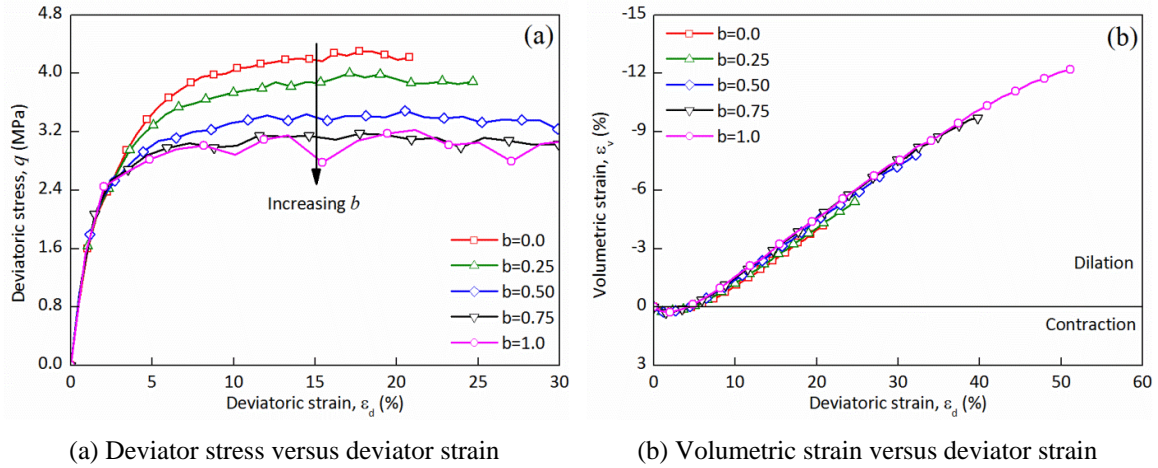


Fig. 8 Simulated behaviors for different  $b$  values with constant mean stress of 2.4 MPa

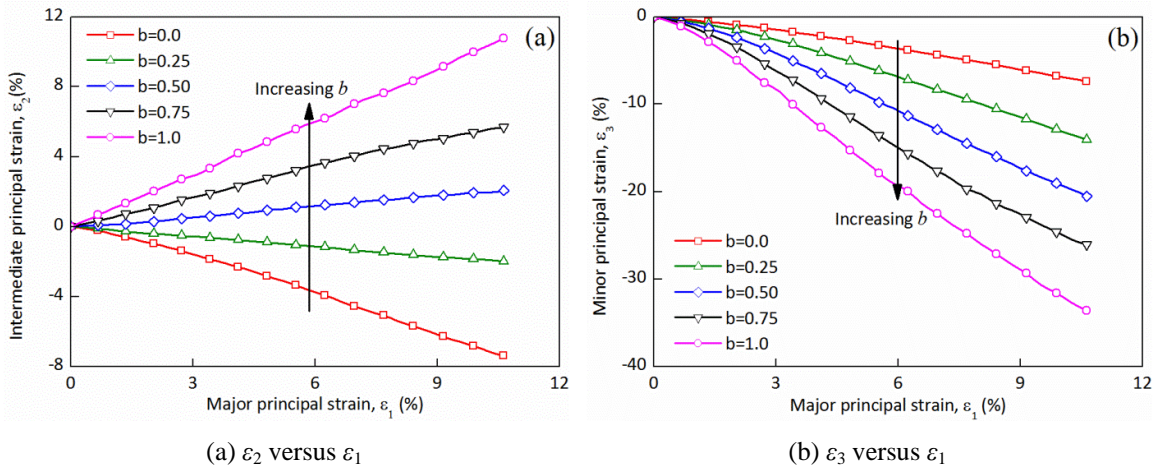


Fig. 9 Relations between principal strains for different  $b$  values

initial tangential slope of the  $q \sim \epsilon_d$  curves, which suggests that the initial shear modulus  $G_0$  seems to be independent of  $b$  (see Fig. 8(a)). Additionally, the evolution of the volumetric strain with the deviator strain shows little influence from the variations in  $b$ , indicating the existence of a one-to-one relationship (mapping correspondence) between the volumetric and deviator strains, irrespective of the value of the principal stress ratio  $b$  (see Fig. 8(b)). The same results were reported by Thornton (2000), Mahmud Sazzad *et al.* (2012), Barreto and O’Sullivan (2012).

In these simulations, together with the work of Thornton (2000), Mahmud Sazzad *et al.* (2012), Barreto and O’Sullivan (2012), slight post-peak strain softening and negligible strength reduction occur after failure, and shear bands are not observed. There are two possible explanations for these results. All simulations are conducted on samples with a slenderness ratio of 1.0. Lade has investigated the influence of the sample slenderness ratio on the occurrence of shear banding; he noted that the shear bands in specimens with  $H/D = 1.0$  always intersect at the lubricated cap and

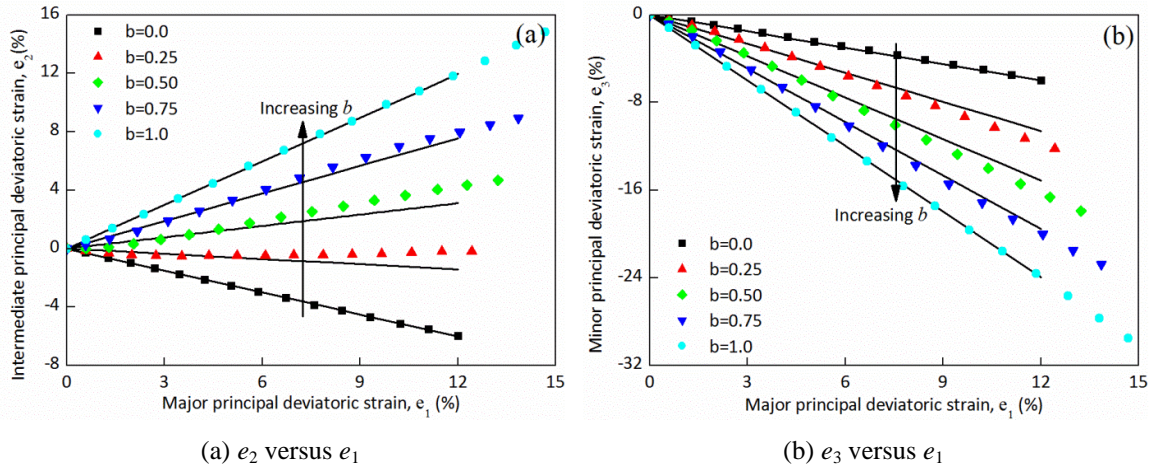


Fig. 10 Relations between principal deviatoric strains for different  $b$  values

base (Lade 2006). The intersection of shear bands with the end platens enhances uniform strains compared with tall specimen, before any gross shear banding develops in the short specimen. The particle interlocking effect, resulting from the irregular particle shapes, provides a more stable micro-structure in the post-peak regime.

The relationship between the principal strains is depicted in Fig. 9. The corresponding relationship for the principal deviatoric strains is shown in Fig. 10. The evolutions of both the minor and intermediate principal strains are nonlinearly related to the major principal strain. The minor principal strain is always extensive, and the rate of expansion increases with increasing  $b$ . The normal strain response in the  $\sigma_2$  direction is highly dependent on the  $b$  value. In the plane strain condition, the sample does not expand or contract in the  $\sigma_2$  direction; the principal stress ratio in this condition is denoted as  $b_{PS}$ . If  $b < b_{PS}$ , the  $e_2$  response is extensive. If  $b > b_{PS}$ , then  $e_2$  demonstrates contractive behavior. By contrast, the corresponding relationship for the principal deviatoric strains is almost linear. The same tendency was reported in Suzuki and Yanagisawa (2006) and Mahmud Sazzad *et al.* (2012). In this study, the relationship between each principal deviatoric strain under a constant mean stress condition can be expressed as follows

$$e_2 = \frac{-3.05b + 1}{-0.06b - 2} e_1 \quad (7)$$

$$e_3 = \frac{3.11b + 1}{-0.06b - 2} e_1 \quad (8)$$

The predicted values based on the above expressions fit well with the simulation results for all variations of  $b$  value.

#### 4.2 Shear dilatancy behavior

The shear dilatancy behavior of the modeled materials is characterized in terms of the stress ratio  $q/p$  and the incremental strain ratio  $d\varepsilon_v/d\varepsilon_d$ . It should be noted that the incremental strains

$d\varepsilon_v$  and  $d\varepsilon_d$  consist of both elastic and plastic components. A fundamental reference for materials that dissipate energy in a frictional mode is presented by Roscoe *et al.* (1963). The dilatancy is simply expressed as

$$d = \frac{d\varepsilon_v^p}{d\varepsilon_d^p} = M - \eta \quad (9)$$

where  $d\varepsilon_v^p$  and  $d\varepsilon_d^p$  are the plastic incremental volumetric and deviator strains,  $\eta = q/p$ , and  $M$  is the stress ratio corresponding to zero dilatancy, also known as the slope of phase transformation line (Chang and Yin 2009).

Rowe analyzed the dilatancy of granular materials and reached the conclusion that the dilatancy parameter  $d$  can be written as (Rowe 1962)

$$d = \frac{d\varepsilon_v^p}{d\varepsilon_d^p} = \frac{9(M - \eta)}{3M - 2M\eta + 9} \quad (10)$$

In Roscoe's stress-dilatancy equation, the rate of change of  $d$  with  $\eta$  is 1, which results in a discrepancy in fitting the experimental results. To address this limitation, a constant  $\lambda$ , such as the constant proposed by Nova (1982), Jefferies (1993), Gajo and Muir Wood (1999), Li *et al.* (1999), and Yang and Muraleetharan (2003), is often added to Eq. (9), which results in

$$d = \frac{d\varepsilon_v^p}{d\varepsilon_d^p} = \lambda(M - \eta) \quad (11)$$

Lagioia *et al.* (1996) proposed a more flexible dilatancy law

$$d = \frac{d\varepsilon_v^p}{d\varepsilon_d^p} = \lambda(M - \eta) \left( \frac{\alpha M}{\eta} + 1 \right) \quad (12)$$

Where  $\alpha$  and  $\lambda$  are parameters. When  $\eta$  tends to zero,  $d$  tends to infinity, which implies a pure volumetric deformation under isotropic loading.

Eqs. (9), (10), (11), and (12) do not consider the effect of density or confining pressure on the dilatancy behavior. Different initial densities are implicitly considered as different material constants (Alonso *et al.* 2007). Additional enhancements of this limitation are included in the work by Cui and Delage (1996), Wan and Guo (1998). A more general approach is to alter the material constants as functions of the density state, e.g., Manzari and Dafalias (1997).

The dilatancy equations and the simulated results for a triaxial compression test ( $b = 0$ ) with constant mean stress of 2.4 MPa are compared in Fig. 11. Using Roscoe's dilatancy Eq. (9), the dilatancy curve is a linear line with a slope of 1. According to Rowe's Eq. (10), the dilatancy curve is slightly nonlinear. The two equations poorly predict the dilative and contractive deformation. The results of the two modified versions of Roscoe's dilatancy Eqs. (11) and (12) compare well with the simulated dilatancy behavior of modeled materials. For its simplicity and acceptable predictive accuracy, Eq. (11) is used to characterize the relation between the stress ratio  $\eta$  and dilatancy parameter  $d$  in the ensuing discussion.

Fig. 12 shows the simulated relationship between the stress ratio and the incremental strain ratio from different stress paths, with a constant mean stress of 2.4 MPa. A linear relation between

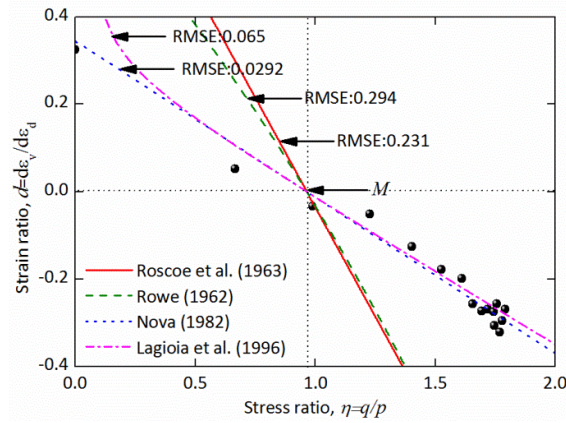


Fig. 11 Dilatancy in Roscoe *et al.* (1963), Rowe (1962), Nova (1982), and Lagioia *et al.* (1996) models

the stress ratio and the incremental strain ratio is observed for all constant  $b$  tests. The stress-dilatancy Eq. (11) is used to fit the simulated results and plotted in each subplot of Fig. 12. The intersection point along the  $\eta$ -axis is labeled  $M$  and corresponds to zero dilatancy. The slope of the line is  $\lambda$ . Values of  $M$  and  $\lambda$  are obtained by the least square fitting of simulated results at different intermediate principal stress ratios. The collective fitting lines in Fig. 12(f) demonstrate that the observed trends from these simulated results vary with the intermediate principal stress ratio  $b$ . As shown in Fig. 12, the characteristic stress ratio  $M$  decreases, while  $\lambda$  increases, with the increasing  $b$  values. Based on the observed trends, the stress-dilatancy behavior of rockfill materials can be described by altering the values of  $M$  and  $\lambda$  in Eq. (11) as functions of the intermediate principal stress ratio. The stress ratio corresponding to zero dilatancy at different Load angles is denoted as  $M^\theta$ . The slope of fitting line at different stress paths is expressed as  $\lambda^\theta$ . Figs. 13(a) and (b) show the variation of  $M^\theta$  and  $\lambda^\theta$ , along with the load angle in the polar coordinate system.  $M^\theta$  and  $\lambda^\theta$ , as functions of the Lode angle  $\theta$ , are expressed as follows

$$M^\theta = M^0 g(\theta) \tag{13}$$

$$\lambda^\theta = \lambda^0 g(\theta) \tag{14}$$

where  $M^0$  and  $\lambda^0$  are values of  $M^\theta$  and  $\lambda^\theta$ , for the Lode angle  $\theta = 0$ .  $g(\theta)$  in Eqs. (13) and (14) is the shape function; it equals 1 when the Lode angle  $\theta = 0$ . A unified shape function  $g(\theta)$  for both  $M^\theta$  and  $\lambda^\theta$  is described as follows

$$g(\theta) = \frac{2K}{(K+1) - (K-1)\sin(3(\theta - \pi/6)) + a\cos^2(3(\theta - \pi/6))} \tag{15}$$

$$\theta = \tan^{-1}\left(\frac{\sqrt{3}b}{2-b}\right)$$

where  $a$  is the fitting parameter,  $K$  is the ratio of characteristic stress ratio in triaxial extension to its counterpart in triaxial compression.

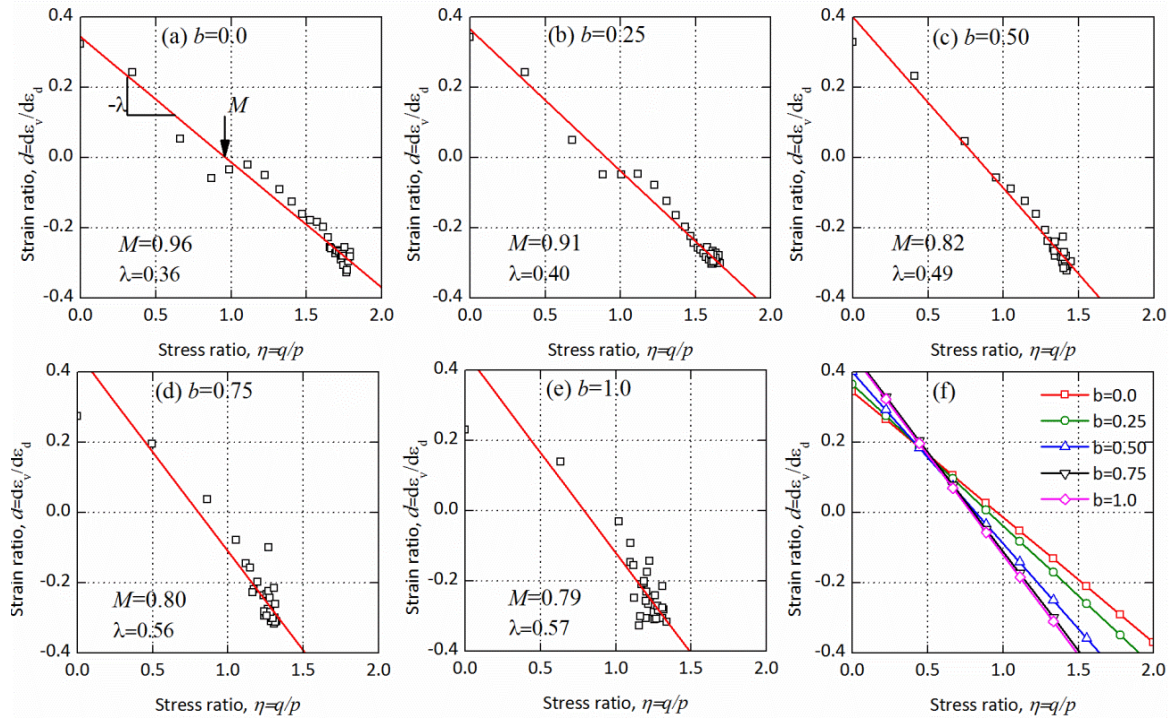


Fig. 12 Stress-dilatancy relations along different stress paths with constant mean stress of 2.4 MPa

#### 4.3 Failure surface

Four strength criteria are used to fit the stress state at failure: Durcker-Prager, Mohr-Coulomb, Matsuoka-Nakai (Matsuoka and Nakai 1974) and Lade-Duncan (Lade and Duncan 1975, Lade 1977). These criteria have been selected because their model parameters can be determined using the triaxial compression test alone. The Lade-Duncan and Matsuoka-Nakia criteria, expressed in terms of stress invariants at failure, are as follows

$$\frac{I_1^3}{I_3} = k_1 \quad (16)$$

$$\frac{I_1 I_2}{I_3} = k_2 \quad (17)$$

where  $I_1$ ,  $I_2$ ,  $I_3$  are the first, second and third invariants of the stress tensor, respectively.  $p_a$  is the atmospheric pressure in the same units as the stress,  $m$  and  $\eta$  are Lade-Duncan parameters determined from triaxial compression tests, and  $k_2$  is the Matsuoka-Nakai parameter.

For each true triaxial test with constant mean stress and  $b$  value, the state of stress corresponding to failure is identified, and the peak friction angle is defined as  $\varphi = \sin^{-1}((\sigma_1 - \sigma_3)/(\sigma_1 + \sigma_3))$ . The peak friction angle as a function of  $b$  is presented in Fig. 14. It is clear from previous DEM simulations and experimental research that the friction angle in triaxial extension is

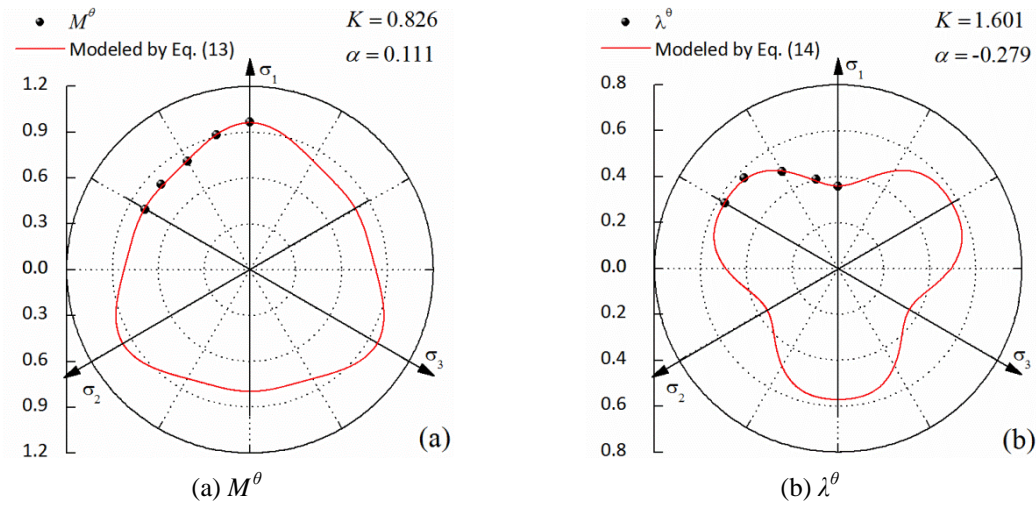


Fig. 13 Comparison of dilatancy parameters between predictions and simulated results

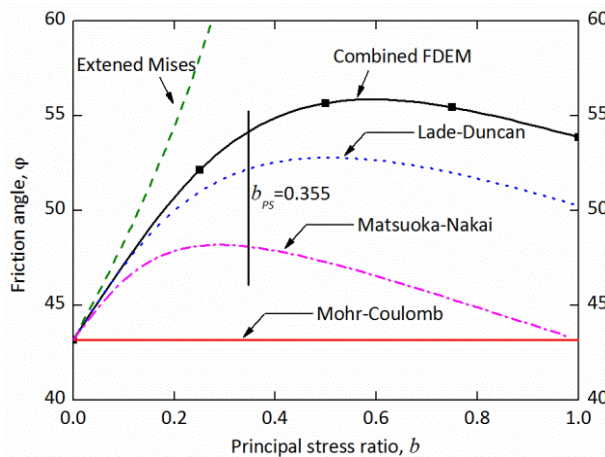


Fig. 14 Evolution of peak friction angle with the intermediate principal stress ratio  $b$

slightly higher than in triaxial compression and a smoothly and non-monotonously varying relation in between. As  $b$  increases from the triaxial compression condition ( $b = 0$ ) to the plane strain condition ( $b_{PS} = 0.355$ ), the friction angle increases. Subsequently, the friction angle continues to increase at a decreasing rate until  $b$  is near 0.68, after which it decreases slowly until  $b$  is 1.0. The shape of the  $\varphi \sim b$  relationship falls into the first category of representative  $\varphi \sim b$  relationships for sands sorted by Lade (2006).

Also shown in Fig. 14 are traces of the above mentioned four criteria. The parameters for these criteria are determined by using the stress state at failure of the triaxial compression condition ( $b = 0$ ). These criteria are then used to predict the friction angles for other constant  $b$  tests. As seen, the Drucker-Prager model grossly overestimates the effect of the intermediate principal stress and may result in non-sensible strength predications, whereas the Mohr-Coulomb model is too conservative,

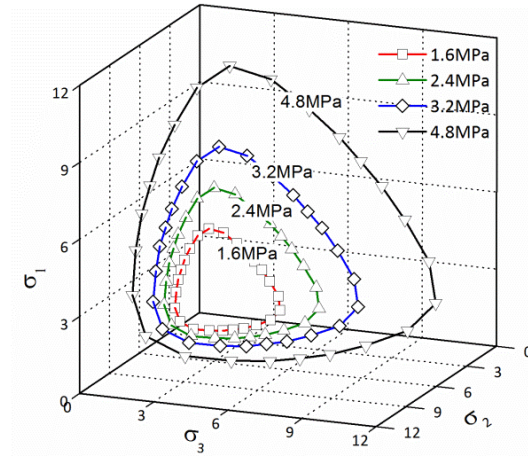
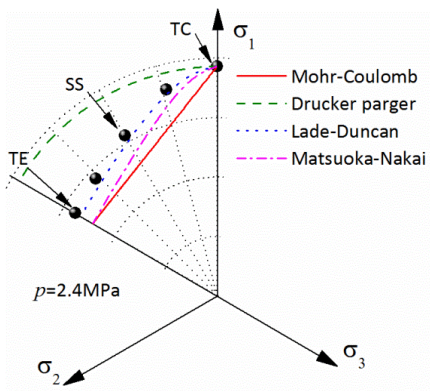
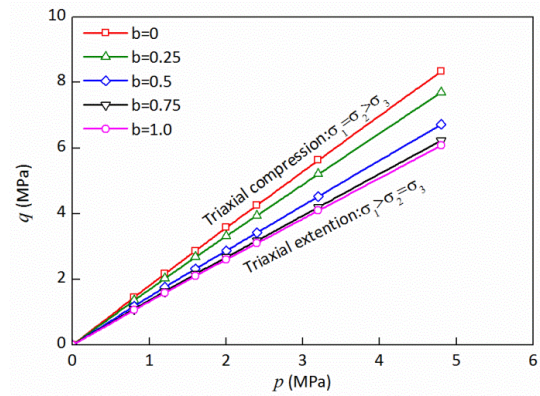


Fig. 15 Failure surface in the principal stress space

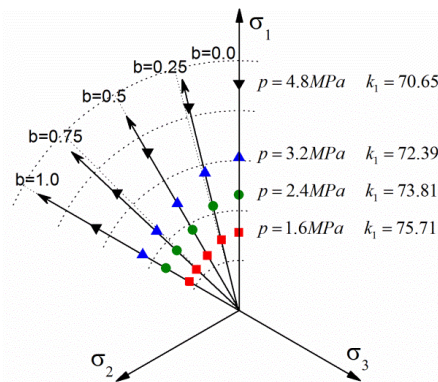


(a) In the deviatoric plane with mean stress of 2.4 MPa

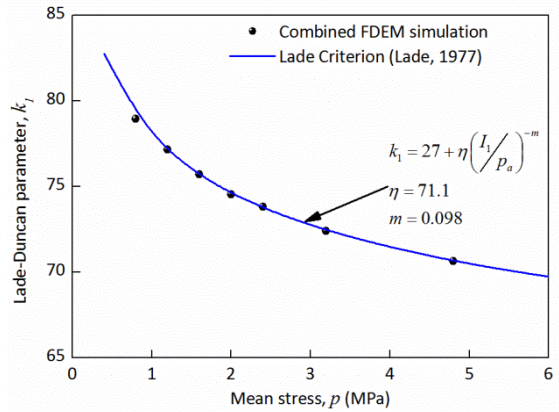


(b) In the  $p$ - $q$  plane

Fig. 16 Trace of failure surface



(a) In the deviatoric plane



(b) In the  $p$ - $q$  plane

Fig. 17 Variation of parameter  $k_1$  with mean stress

because it neglects the strengthening effect of intermediate principal stress. Consequently, both models have poor predictive capability of the shear strength of rockfill materials. However, the LD and MN models account for the effect of the intermediate principal stress on the shear strength, and show relatively good predictive capability, but both models underestimate the friction angles.

The stress states at failure for different constant- $b$  and constant- $p$  tests are plotted in the principal stress space (see Fig. 15). As seen, the failure surface is smooth and plots as a convex cone. The projection of the failure surface on the deviatoric plane, based on different constant  $b$  tests with a mean stress of 2.4 MPa is shown in Fig. 16(a). The trace of the failure surface on the deviatoric plane is not circular, but a convex curvilinear triangle; the coordinate of the surface from the hydrostatic axis depends on the  $b$  values, thus showing the stress path dependency. Among the four strength criteria, the Lade-Duncan provides the closest match with the combined FEM/DEM simulation results. The failure surface superimposed on the meridian plane is a curved line, which bends down along with the increase of the mean stress (see Fig. 16(b)). The Mohr-Coulomb, Drucker-Prager, and Matsuoka-Nakai criteria are not capable of capturing the curved shape of the failure surface on the meridian plane. The additional enhancements of these three criteria are not in the scope of this discussion. The exponential term  $m$  in the Lade-Duncan criterion allows for the consideration of the nonlinear strength in the meridian plane (Lade 1977). Figs. 17(a) and (b) shows the  $p \sim k_1$  relationship, where  $p$  is the mean stress and  $k_1$  is the Lade-Duncan parameter determined by stress state at failure obtained from the triaxial compression condition of each constant- $p$  test. The expression in Eq. (16) is then used to fit this relation, and parameters  $m$  and  $\eta$  are derived by a least square approach. As shown, the Lade-Duncan criterion can capture the curvature of the failure surface.

## 5. Conclusions

Using combined FDEM modeling of true triaxial tests, an alternative way to evaluate the mechanical behavior of rockfill materials has been presented. The stress-strain characteristics, stress-dilatancy behavior and failure surface of rockfill materials under three-dimensional stress conditions are presented separately. The primary findings drawn from this qualitative study are the following:

- The stress-strain behavior becomes increasingly stiff, and both the deviator stress and the axial strain to failure decrease with the increasing  $b$  values. There is a small difference in the initial tangential slope of the  $q \sim \varepsilon_d$  curves, which suggests that the initial shear modulus is independent of  $b$ . Additionally, the evolution of the volumetric strain with the deviator strain is not significantly influenced by the variations in  $b$ .
- A linear relation between the stress ratio and the incremental strain ratio is observed for all constant- $b$  tests. The trends observed from these simulated results vary with the intermediate principal stress ratio  $b$ .
- Comparison of the four existing dilatancy functions indicates that the two modified versions of Roscoe's dilatancy Eqs. (11) and (12) compare well with the simulated dilatancy behavior of modeled materials. For its simplicity and acceptable predictive accuracy, Eq. (11) is used to characterize the shear dilatancy behavior, and a shape function is added into Eq. (11) to reflect the influence of the intermediate principal stress.
- The shape of the  $\varphi \sim b$  relationship falls into the first category of representative  $\varphi \sim b$  relationships for sands sorted by Lade. The failure surface is smooth and plots as a convex

cone. The trace of the failure surface on the deviatoric plane is not circular but a convex curvilinear triangle, and the coordinate of the surface from the hydrostatic axis depends on the  $b$  values, which shows the stress path dependency. The failure surface superimposed on the meridian plane is a curved line, which bends downward with the increase of the mean stress. Among the four strength criteria, the Lade criterion provides the closest match to the combined FDEM simulation results.

## Acknowledgments

This work was supported by the National Natural Science Foundation of China (Grant No. 51379161 and 51322905).

## References

- Alonso, E.E., Iturralde, E.F.O. and Romero, E.E. (2007), "Dilatancy of coarse granular aggregates", *Exp. Unsat. Soil Mech.*, **112**, 119-135.
- Barreto, D. and O'Sullivan, C. (2012), "The influence of inter-particle friction and the intermediate stress ratio on soil response under generalised stress conditions", *Granul. Matter.*, **14**(4), 505-521.
- Chang, C.S. and Yin, Z.Y. (2009), "Modeling stress-dilatancy for sand under compression and extension loading conditions", *J. Eng. Mech.*, **136**(6), 777-786.
- Cheng, Z.L., Zuo, Y.Z. and Ding, H.S. (2010), "Wetting characteristics of coarse-grained materials", *Chin. J. Geotech. Eng.*, **32**(2), 243-247.
- Cui, Y.J. and Delage, P. (1996), "Yielding and plastic behaviour of an unsaturated compacted silt", *Geotechnique*, **46**(2), 291-311.
- Cundall, P.A. and Hart, R.D. (1992), "Numerical modelling of discontinua", *Eng. Computation.*, **9**(2), 101-113.
- Gajo, A. and Wood, M. (1999), "Severn-trent sand: A kinematic-hardening constitutive model: The  $q-p$  formulation", *Geotechnique*, **49**(5), 595-614.
- Jefferies, M.G. (1993), "Nor-Sand: A simple critical state model for sand", *Geotechnique*, **43**(1), 91-103.
- Lade, P.V. (1977), "Elasto-plastic stress-strain theory for cohesionless soil with curved yield surfaces", *Int. J. Solids Struct.*, **13**(11), 1019-1035.
- Lade, P.V. (2006), "Assessment of test data for selection of 3-D failure criterion for sand", *Int. J. Numer. Anal. Meth. Geomech.*, **30**(4), 307-333.
- Lade, P.V. and Duncan, J.M. (1975), "Elastoplastic stress-strain theory for cohesionless soil", *J. Geotech. Eng. Div.*, **101**(10), 1037-1053.
- Lagioia, R., Puzrin, A.M. and Potts, D.M. (1996), "A new versatile expression for yield and plastic potential surfaces", *Comput. Geotech.*, **19**(3), 171-191.
- Li, X.S., Dafalias, Y.F. and Wang, Z.L. (1999), "State-dependant dilatancy in critical-state constitutive modelling of sand", *Can. Geotech. J.*, **36**(4), 599-611.
- Mahmud Sazzad, M., Suzuki, K. and Modaressi-Farahmand-Razavi, A. (2012), "Macro-Micro Responses of Granular Materials under Different  $b$  Values Using DEM", *Int. J. Geomech.*, **12**(3), 220-228.
- Manzari, M.T. and Dafalias, Y.F. (1997), "A critical state two-surface plasticity model for sands", *Geotechnique*, **47**(2), 255-272.
- Matsuoka, H. and Nakai, T. (1974), "Stress-deformation and strength characteristics of soil under three different principal stresses", *Proceedings of Japan Society of Civil Engineers (4th Edition)*, **232**, 59-70.
- Munjiza, A. (2004), *The Combined Finite-Discrete Element Method*, John Wiley & Sons, Ltd., Chichester, UK.
- Munjiza, A., Owen, D.R.J. and Bicanic, N. (1995), "A combined finite-discrete element method in transient

- dynamics of fracturing solids”, *Eng. Computation.*, **12**(2), 145-174.
- Ng, T.T. (2004), “Macro-and micro-behaviors of granular materials under different sample preparation methods and stress paths”, *Int. J. Solids Struct.*, **41**(21), 5871-5884.
- Ng, T.T. (2005), “Behavior of gravity deposited granular material under different stress paths”, *Can. Geotech. J.*, **42**(6), 1644-1655.
- Nova, R. (1982), “A constitutive model for soil under monotonic and cyclic loading”, *Soil Mech.- Trans. Cycl. Load.*, John Wiley & Sons Ltd., 343-362.
- Procopio, A.T. and Zavalianos, A. (2005), “Simulation of multi-axial compaction of granular media from loose to high relative densities”, *J. Mech. Phys. Solids*, **53**(7), 1523-1551.
- Roscoe, K.H., Schofield, A. and Thurairajah, A. (1963), “Yielding of clays in states wetter than critical”, *Geotechnique*, **13**(3), 211-240.
- Rothenburg, L. and Bathurst, R.J. (1989), “Analytical study of induced anisotropy in idealized granular materials”, *Geotechnique*, **39**(4), 601-614.
- Rowe, P.W. (1962), “The stress-dilatancy relation for static equilibrium of an assembly of particles in contact”. *Proceedings of the Royal Society of London, Series A (4th Edition)*, **269** (1339), 500-527.
- Sun, D.A., Huang, W. and Yao, Y. (2008), “An experimental study of failure and softening in sand under three-dimensional stress condition”, *Granul. Matter.*, **10**(3), 187-195.
- Suzuki, K. and Yanagisawa, E. (2006), “Principal deviatoric strain increment ratios for sand having inherent transverse isotropy”, *Int. J. Geomech.*, **6**(5), 356-366.
- Thornton, C. (2000), “Numerical simulations of deviatoric shear deformation of granular media”, *Geotechnique*, **50**(1), 43-53.
- Wan, R.G. and Guo, P.J. (1998), “A simple constitutive model for granular soils: modified stress-dilatancy approach”, *Comput. Geotech.*, **22**(2), 109-133.
- Xiao, Y., Liu, H.L., Zhu, J.G. and Shi, W.C. (2011), “Dilatancy equation of rockfill material under the true triaxial stress condition”, *Sci. China Tech. Sci.*, **54**(1), 175-184.
- Yang, Y. and Muraleetharan, K.K. (2003), “The middle surface concept and its application to the elasto-plastic behaviour of saturated sands”, *Geotechnique*, **53**(4), 421-431.